Acta Oceanol. Sin., 2017, Vol. 36, No. 7, P. 39–47
DOI: 10.1007/s13131-017-1082-3
http://www.hyxb.org.cn
E-mail: hyxbe@263.net

A numerical simulation of latent heating within Typhoon Molave

LIU Yang[1, 2, 3], LIN Wenshi[1]*, LI Jiangnan[1], WANG Gang[2], YANG Song[1], FENG Yerong[3]

[1] School of Atmospheric Sciences, Sun Yat-sen University, Guangzhou 510275, China

[2] Meteorological Center of Middle South Regional Air Traffic Management Bureau of Civil Aviation of China, Guangzhou 510470, China

[3] Guangdong Provincial Key Laboratory of Regional Numerical Weather Prediction, China Meteorological Administration, Guangzhou 510080, China

Received 13 December 2016; accepted 17 January 2017

Abstract

The weather research and forecasting (WRF) model is a new generation mesoscale numerical model with a fine grid resolution (2 km), making it ideal to simulate the macro- and micro-physical processes and latent heating within Typhoon Molave (2009). Simulations based on a single-moment, six-class microphysical scheme are shown to be reasonable, following verification of results for the typhoon track, wind intensity, precipitation pattern, as well as inner-core thermodynamic and dynamic structures. After calculating latent heating rate, it is concluded that the total latent heat is mainly derived from condensation below the zero degree isotherm, and from deposition above this isotherm. It is revealed that cloud microphysical processes related to graupel are the most important contributors to the total latent heat. Other important latent heat contributors in the simulated Typhoon Molave are condensation of cloud water, deposition of cloud ice, deposition of snow, initiation of cloud ice crystals, deposition of graupel, accretion of cloud water by graupel, evaporation of cloud water and rainwater, sublimation of snow, sublimation of graupel, melting of graupel, and sublimation of cloud ice. In essence, the simulated latent heat profile is similar to ones recorded by the Tropical Rainfall Measuring Mission, although specific values differ slightly.

Key words: latent heat, weather research and forecasting model, Typhoon Molave, thermodynamic structure, cloud microphysics, zero degree isotherm

Citation: Liu Yang, Lin Wenshi, Li Jiangnan, Wang Gang, Yang Song, Feng Yerong. 2017. A numerical simulation of latent heating within Typhoon Molave. Acta Oceanologica Sinica, 36(7): 39–47, doi: 10.1007/s13131-017-1082-3

1 Introduction

Latent heat is released or absorbed in the atmosphere as a result of phase changes of water (i.e., gas to liquid, gas to solid, liquid to solid, or vice versa). These phase changes involve processes of condensation, evaporation of cloud water and rainwater, freezing of raindrops and cloud water, melting of cloud ice, snow and graupel/hail, as well as deposition and sublimation of cloud ice (Tao et al., 2006). Riehl and Malkus (1958) emphasize that the latent heat is the primary fuel source of a tropical convective heat engine. Emanuel (1999) studied thermodynamic controls of a hurricane intensity, identifying three important factors for the evolution of the hurricane intensity: a storm's initial intensity, the thermodynamic state of the atmosphere, and a heat exchange with the oceanic upper layer. Generally, the release of latent heat from the transformation of different hydrometeors is an important energy source for typhoons. Zhang and Kieu (2006) show that the release of the latent heat in the eyewall plays an important role in divergence aloft and convergence below the hurricane eye. Wu et al. (2009) also show that diabatic heating is a key factor to eyewall development in tropical cyclones. It is estimated that a tropical cyclone releases heat energy at a rate of 0.60×10^{15} W (2×10^{18} J/h), assuming that an average hurricane produces 1.5 cm/d of rain inside a circle of radius 665 km (Gray, 1981). Another value of the latent heat release of 0.88×10^{15} W was calculated by Adler and Rodgers (1977). From special sensor microwave/imager (SSM/I), Wang et al. (2008) indicate that the mean total latent heat released from a developing tropical disturbance is larger than for a non-developing tropical disturbance.

The latent heat is an energy released or absorbed during a constant-temperature process with phase changes. These phase changes involve phase of cloud water, rainwater, cloud ice, snow and graupel, etc. Latent heating (LH) cannot be directly measured using current technologies (Tao et al., 2006). Moreover, there has been no dependable method for observing the global distribution of diabatic heating. This is particularly true over ocean areas, because of the lack of adequate conventional data sets. However, the diabatic heating can be derived using a residual method (called a diagnostic budget) based on vertical profiles of temperature and three-dimensional wind fields, available from widespread rawinsonde networks (Yanai et al., 1973; Johnson, 1984; Houze, 1997). Fortunately, satellite measurements from the Tropical Rainfall Measuring Mission (TRMM) provide a more reliable method for detecting the LH. Thus, the LH can be estimated using data from SSM/I. In fact, several investigators (Olson et al., 1999; Tao et al., 1993; Yang and Smith, 1999) have

Foundation item: The National Key Basic Research Program of China under contract No. 2014CB953904; the Natural Science Foundation of Guangdong Province under contract No. 2015A030311026; the National Natural Science Foundation of China under contract Nos 41275145 and 41275060.

*Corresponding author, E-mail: linwenshi@mail.sysu.edu.cn

successfully used this method. However, the TRMM microwave imager (TMI), launched in 1997, has a finer spatial resolution than the SSM/I. Thus, the LH is now retrieved from cloud-resolving models (CRMs), supported by the TRMM rainfall products (Kummerow et al., 2001).

Although there is lots of research on tropical cyclones, few studies have examined inner-core energy conversions because of the lack of high-resolution data. To calculate the LH, research efforts have focused almost exclusively on TRMM satellite retrieval. Moreover, there are a few studies using numerical simulations to determine LH calculations (Hogsett and Zhang, 2009; Sui et al., 1994). In this study, we aimed at understanding more about the LH structure during a typhoon evolution. Specifically, this would enable us to calculate typhoon LH using the microphysical LH budgets from the Weather Research and Forecasting (WRF) single-moment six-Class (WSM6) microphysical scheme (Hong et al., 2009). To study the LH structure of a typhoon core, the WRF model with the WSM6 cloud microphysical scheme was used to simulate Typhoon Molave. Here, emphasis was placed on revealing the LH structure and processes occurring within this typhoon, through the calculation of LH rates of various cloud microphysical processes. Our detailed analysis of Typhoon Molave is presented here as a case study.

2 Synoptic overview of Typhoon Molave

Typhoon Molave began as a tropical depression that originated east of the Philippines at 00:00 UTC on 15 July 2009. Moving northwestward, it was upgraded to a tropical storm, east of the Philippines at 06:00 UTC on 16 July. It strengthened to become a typhoon over the South China Sea, tracking west-northwest from 17:00 UTC to 18:00 UTC on 17 July. It reached its peak intensity at 18:00 UTC, with maximum surface winds of 33 m/s and central pressure of 975 hPa. Typhoon Molave made landfall on Shenzhen City, China. Subsequently, it weakened rapidly, and was downgraded to a tropical depression at 06:00 UTC on 19 July, before dissipating 6 h later over southern China.

3 Experiment setup

In this study, the advanced research WRF (ARW) dynamical core (Version 3.2) (Skamarock et al., 2005) was used to simulate Typhoon Molave. The ARW 3.2 solves the fully compressible, non-hydrostatic Euler equations of motion in flux with terrain, following sigma coordinates. Our simulation was carried out on an Arakawa C-grid with triple-nested domains (D01, D02, and D03). A Mercator map projection with horizontal grid spacing of 18, 6, and 2 km was configured for the WSM6 simulation (Fig. 1). Domain D01 is the outermost mesh domain, with its center located at 19°N and 119°E, and a grid spacing of 18 km; it was set up to simulate the large-scale environmental field of the typhoon. The intermediate domain, D02, was used to simulate mesoscale features of the typhoon evolution; it has a grid spacing of 6 km. The fine domain, D03, was designed for detailed analysis of small-scale structures and microphysical processes of the typhoon; it has a grid spacing of 2 km. From the ground surface to the top layer, there were 28 vertical levels defined within the WRF model. The following parameterizations were activated for all three domains: the WSM6 cloud microphysics scheme, based on Hong and Lim (2006); the Yonsei University boundary layer parameterization, which accounts for local and nonlocal mixing (Hong et al., 2006); the Dudhia short wave parameterization (1989); and the rapid radiative transfer model (RRTM) long-wave parameterization (Mlawer et al., 1997). The Betts-Miller-Janjic cumulus parameterization scheme (Betts, 1986; Janjić, 1994) was

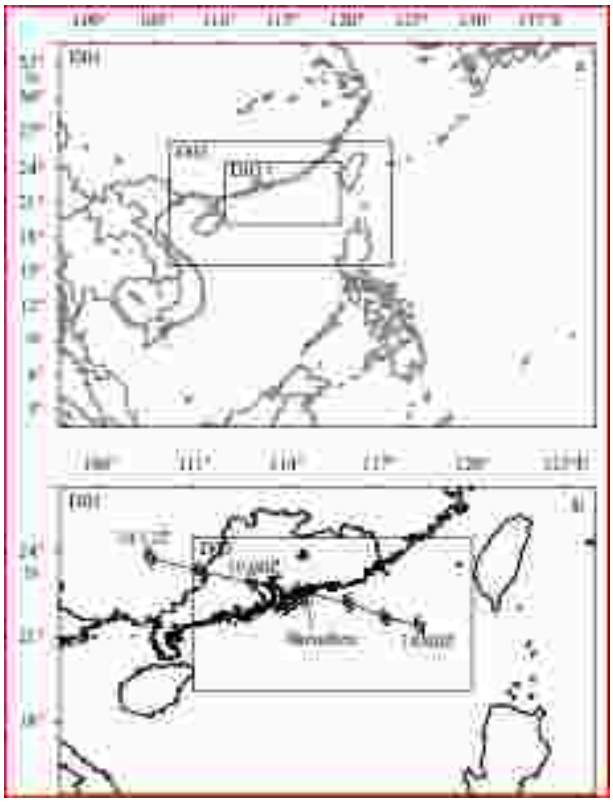

Fig. 1. The setting of the three domains used for the model. a. Nested domains for 18 km (D01), 6 km (D02), 2 km (D03) grid spacing. b. The best track of Typhoon Molave in Domains D02 and D03, for the period from 00:00 UTC on 18 July to 12:00 UTC on 19 July 2009. The best track (observed typhoon track) data are from the China Meteorological Administration. 19/12Z represents 12:00 on 19 July, 19/00Z 00:00 on 19 July, and 18/00Z 00:00 on 18 July.

used in Domains D01 and D02. Meanwhile, no cumulus parameterization scheme was used in Domain D03 (Molinari and Dudek, 1992; Lin et al., 2011), because convection is assumed to be resolved reasonably well by the explicit microphysical parameterization scheme. The initial and boundary conditions were interpolated horizontally for the coarse model resolution (with a grid spacing 18 km), and vertically to 28 levels using the US National Center for Environmental Prediction (NCEP) final reanalysis (FNL) data (http://dss.ucar.edu/datasets/ds083.2). The FNL data sets are compiled at 6 h interval, with a horizontal grid resolution of 1°×1°. Surface and rawinsonde conventional observation data were incorporated into our analysis using a Cressman-type analysis technology (Benjamin and Seaman, 1985). QuikSCAT/NCEP blended ocean winds data were also accessed from Colorado Research Associates (5.0) (http://dss.ucar.edu/datasets/ds744.4), and incorporated using the standard MM5 (mesoscale model; developed by the Pennsylvania State University and the National Center for Atmospheric Research) initialization procedure. A bogus vortex with a maximum velocity of 60 m/s and a maximum radius of 190 km (Low-Nam and Davis, 2001; Fong et al., 2001) was inserted into Domain D01. Initial conditions for Domains D02 and D03 were obtained from interpolation of Domain D01 values. For Domains D01 and D02, the WSM6 experiment was initialized at 00:00 UTC on 18 July, and was integrated for 36 h. Over the integration time, the best track of Typhoon Molave was located in Domain D02. In Domain D03, integration

was preformed from 00:00 UTC on 18 July to 00:00 UTC on 19 July.

4 Simulated results

4.1 *Primary heading, intensity, and precipitation amounts*

In general, the simulated track followed the observed track for the entire 36 h period. Figure 2a shows 6 h simulated and observed typhoon tracks, while Fig. 2b shows 6 h track error. The simulated Typhoon Molave made landfall around 18:00 UTC on 18 July; the landfall location error was less than 33 km. After landfall, the simulated track was slightly northward of the observed track, having a maximum error of 72 km. In conclusion, the simulated track of Molave was similar to the observed with small error, which indicated that a control experiment has a good representation of typhoon track.

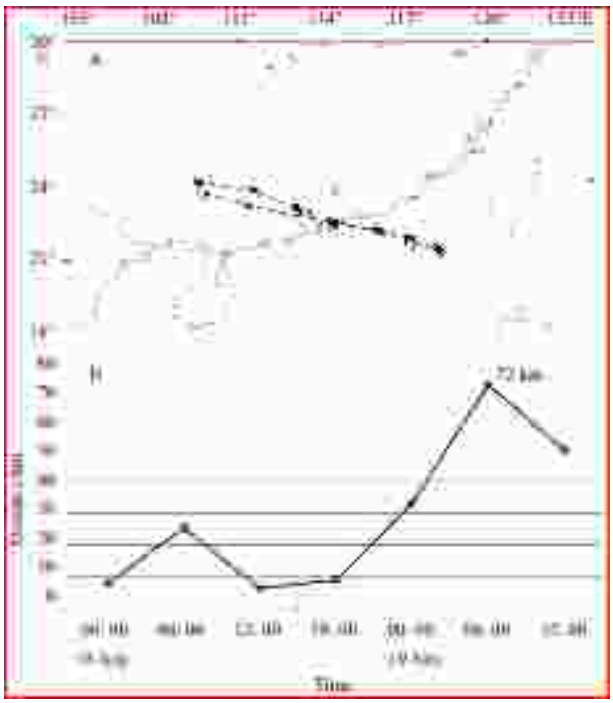

Fig. 2. The 6 h tracks of Typhoon Molave showing the best track (open typhoon symbols), and the simulation (solid typhoon symbols), from 00:00 UTC on 18 July to 12:00 UTC on 19 July, 2009 in the Domain D02 (a); and the track error of the simulation, compared with the best track for this period (b).

Figures 3a and b show the minimum sea-level pressure (MSLP) and maximum surface wind (MSW) for both the simulated and observed tracks of Typhoon Molave. The simulation data were from the inner model domain (D03) for the period from 00:00 UTC on 18 July to 00:00 UTC on 19 July, and from D02 for the period from 03:00 to 12:00 UTC on 19 July. Comparison shows that the simulated MSLPs were 20 hPa higher than those observed, over almost the whole simulation period. From 06:00 UTC on 18 July to 12:00 UTC on 19 July, the simulated MSWs were less than observed values. Overall, the MSW and MSLP of a control experiment went well with the observed.

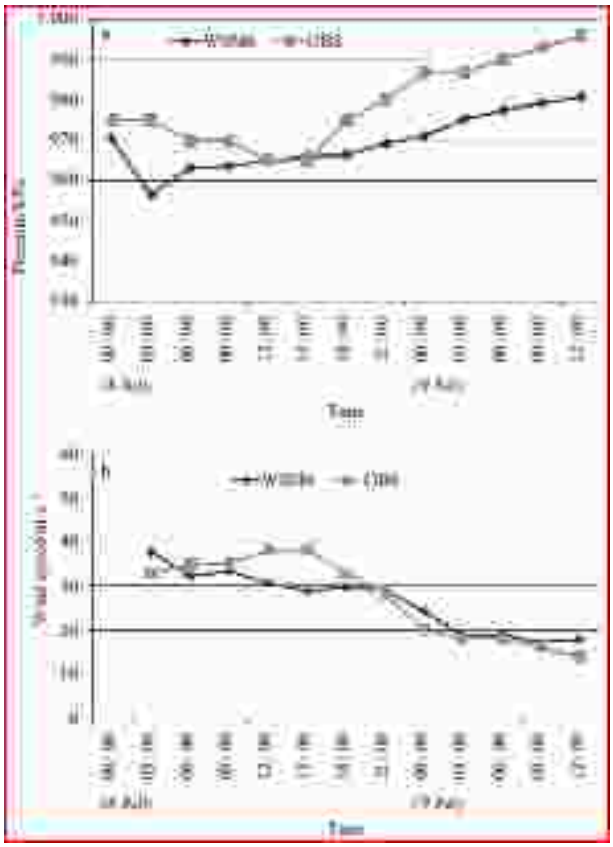

Fig. 3. Time series showing the minimum central pressures (a) and maximum surface winds (b) of Typhoon Molave from the 60 h simulation and their corresponding observations for the same period.

Figures 4 and 5 show the simulated and observed precipitation amounts (mm), respectively. For the two periods from 00:00 to 06:00 UTC (Figs 4a and b) and from 06:00 to 12:00 UTC (Figs 4c and d) on 18 July, with the typhoon rain band located to the east of Guangdong Province, China, the simulated 6 h accumulated

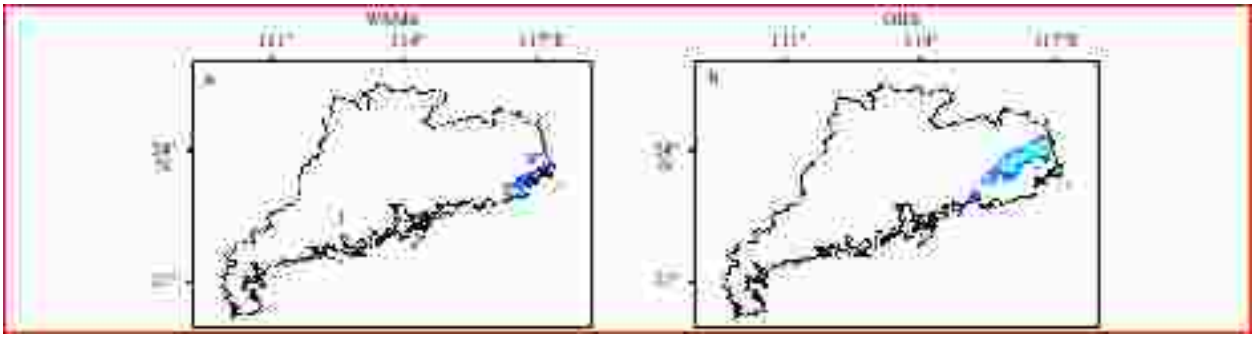

Fig. 4

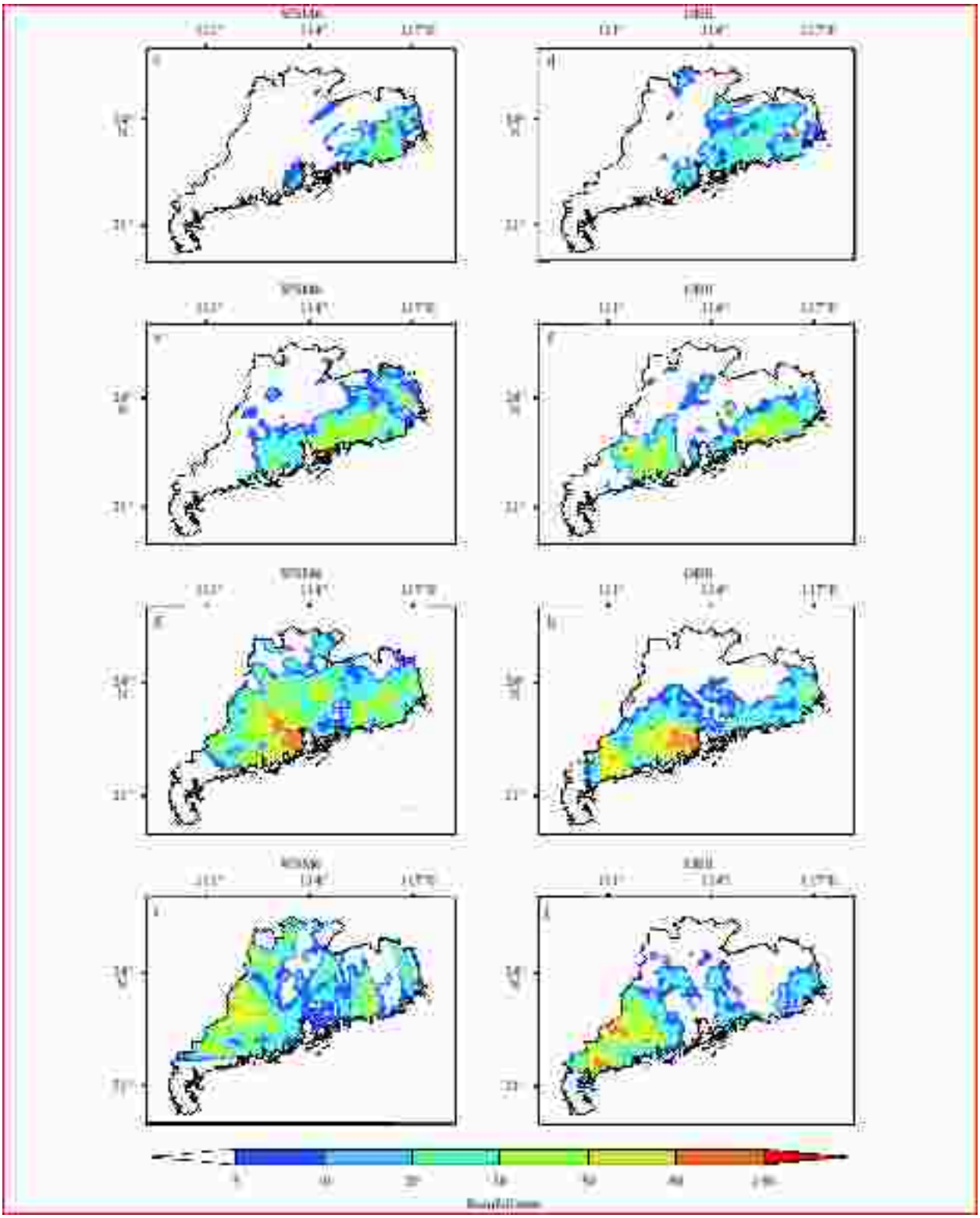

Fig. 4. The 6 h accumulative rainfall for Guangdong Province related to Typhoon Molave for various periods: from 00:00 UTC on 18 July to 06:00 UTC on 18 July for the simulation (a) and the observations (b); from 06:00 UTC on 18 July to 12:00 UTC on 18 July for the simulation (c) and the observations (d); from 12:00 UTC on 18 July to 18:00 UTC on 18 July for the simulation (e) and the observations (f); from 18:00 UTC on 18 July to 00:00 UTC on 19 July for the simulation (g) and the observations (h); and from 00:00 UTC on 19 July to 06:00 UTC on 19 July for the simulation (i) and the observations (j). The observed data are from the China Meteorological Administration. The black line defines the administrative boundaries of Guangdong Province.

rain amount was small, and in good agreement with observations. From 12:00 to 18:00 UTC (Figs 4e and f), the simulated 6-h rain accumulation was slightly less than observed amounts in the western part of Guangdong, although there is reasonable agree-

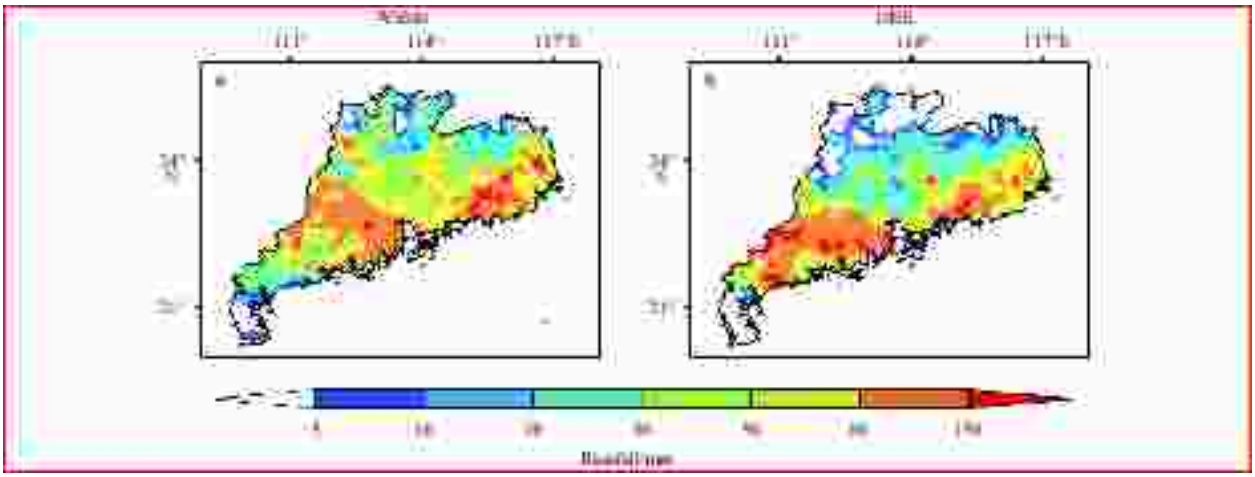

Fig. 5. The 36 h accumulative rainfallin Guangdong Province related to Typhoon Molave for the simulation (a) and the observation (b) from 00:00 UTC on 18 July to 12:00 UTC on 19 July, 2009. The observed data are from the China Meteorological Administration.

ment with observations from the eastern part of Guangdong. From 18:00 UTC on 18 July to 00:00 UTC on 19 July (Figs 4g and h), the maximum observed precipitation exceeded 80 mm, which was also simulated in our model. From 00:00 to 06:00 UTC on 19 July (Figs 4i and j), the spatial distribution of the simulated precipitation was reasonably consistent with that observed. Therefore, over the 36 h period, the simulated accumulated precipitation amount and the spatial distribution of the accumulated precipitation were similar to those observed (Figs 5a and b). However, the 36 h accumulated rainfall from our simulation shows more rain fell over the central part of the model domain.

4.2 *Vertical kinematic and thermodynamic structures*

To show kinematic and thermodynamic structures in the eye wall of Typhoon Molave, east-west cross-sections of the simulated values were constructed. Here, horizontal and vertical wind speeds (m/s), radar reflectivity, and five types of hydrometer distributions are displayed in Figs 6a–e, respectively. The hydrometer types included cloud water, rainwater, cloud ice, snow, and graupel. These cross-sections represent structures occurring at 12:00 UTC on 18 July. They were generated at a reference latitude (22.25°N), passing through the storm center (Pattnaik and Krishnamurti, 2007). The analyzed range was 200 km from the center to the western or eastern extremity, covering Domain D03; while the vertical levels represent the ground surface to 16 km height.

The east-west cross-sections of the horizontal wind speed show maximum wind speeds in the core of ca. 35 m/s (Fig. 6a). There is a “no wind zone” in the typhoon center, about 100 km wide. The maximum wind range in the eastern half of the eye wall is greater than in its western half. Figure 6b shows the vertical velocity field, in which the negative values are shown as dot-dash contours. There is a narrow strip of strong upward motion,

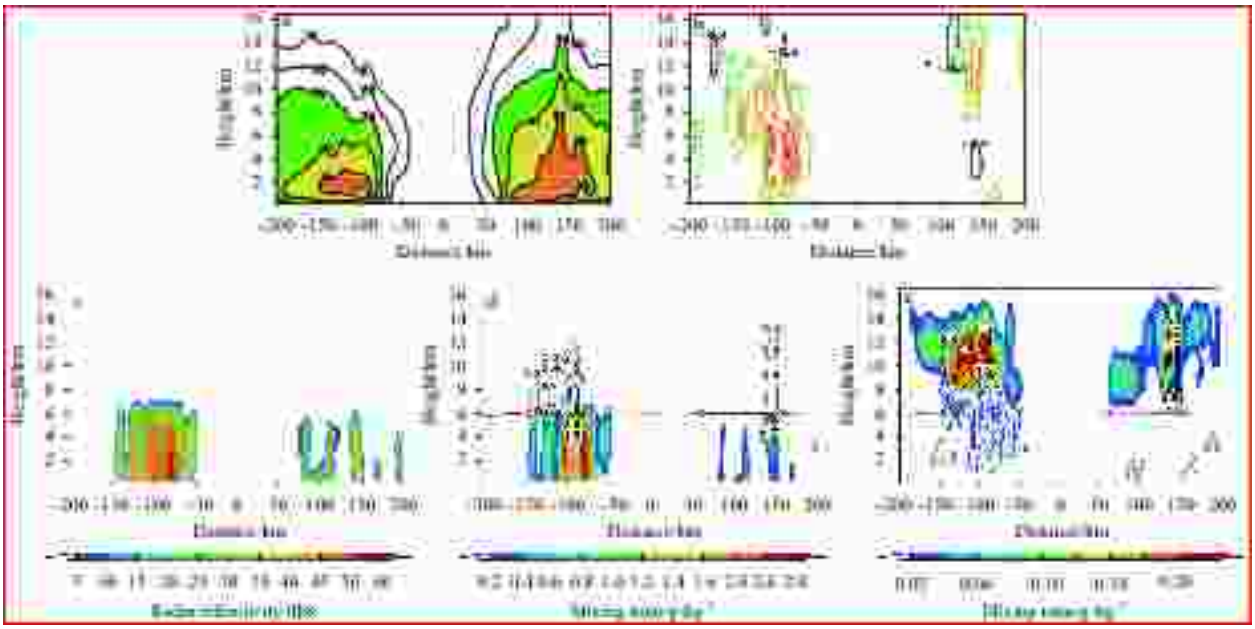

Fig. 6. An east-west cross-section through the center of Typhoon Molave at 12:00 UTC on 18 July 2009 showing simulation results for various variables: a. horizontal wind speed (m/s), with a contour interval of 5 m/s; b. vertical velocity (m/s), with a contour interval of 0.4 m/s; c. radar reflectivity; d. graupel and rainwater mixing ratio, with a contour interval of 0.2 g/kg; and e. cloud ice (shaded), snow (solid contours), and cloud water mixing ratio, with a contour interval of 0.3 g/kg.

with velocity of 0.4–3.0 m/s, near the western part of the storm eye wall, and weak upward motion in its eastern part. The upward motion in the western part of the eye wall extends vertically from the surface to a height of 14 km. Regions of strong downward motion (shaded) are located further away, on either side of the eye wall, having a minimum value of –0.4 m/s. Figure 6c shows that the radar reflectivity is greater than 40 dBz close to the eye wall. There is little reflectivity above 7 km, because of an equivalent reflectivity factor related to the densities and exponential size distributions of raindrops, snow particles, and graupel particles within the column. Figure 6d shows the simulated graupel (contours) and rainwater (shaded) mixing ratios. The graupel mixing ratio varies between 0.2 and 1.6 g/kg, but shows that graupel concentrates near the inner eye wall and above the zero degree isotherm. Rainwater is mostly found below the zero degree isotherm, and is correlated with graupel hydrometeors. This suggests that the main source of rainwater is linked to graupel. Figure 6e displays east-west cross-sections of snow (black contours), cloud ice (shaded), and cloud water mixing ratios (blue contours). There is an accumulation of these hydrometeors near the eye wall. The cloud ice mixing ratio is maximal above the zero degree isotherm, with a maximum value of 0.24 g/kg. The snow mixing ratio also is maximal above the zero degree isotherm. Cloud water extends from the surface to a height of 8 km. This indicates that there is abundant supercooled water above the zero degree isotherm, corresponding to high mixing ratios of graupel and rainwater.

4.3 *The cloud microphysical latent heating structure of the typhoon core*

The LH from microphysical phase changes of water (i.e., liquid to solid, gas to liquid, gas to solid or vice versa) can be explicitly calculated in the WRF model (Sui et al., 1994), as follows:

$$LH = \frac{1}{c_p}\left[L_v\,(c-e) + L_f\,(f-m) + L_s\,(d-s)\right], \tag{1}$$

where c_p represent the specific heat at constant pressure; L_v, L_f, and L_s are the latent heats of condensation, freezing, and sublimation, respectively; and the variables c, e, f, m, d, and s denote rates for (1) condensation of cloud water; (2) evaporation of cloud water and rainwater; (3) freezing of cloud water and rainwater; (4) melting of cloud ice, snow, and graupel; (5) deposition of cloud ice; and (6) sublimation of all solid hydrometeors, respectively.

4.3.1 *The vertical structure of latent heat*

Figure 7a shows an east-west cross-section of the simulated total LH rate, while Figs 7b to d show east-west cross-sections of the LH rates of condensation and evaporation, freezing and melting, and deposition and sublimation, respectively. It is clear from the vertical structure of the latent heat that no convective motion occurs within the typhoon eye. The total LH rate in the western part of the typhoon is much higher than in the eastern part, indicating a stronger convection in the western part. The maximum total LH rate is about 40–50°C /h. The LH rate for condensation and evaporation contributes the most to the total LH rate,

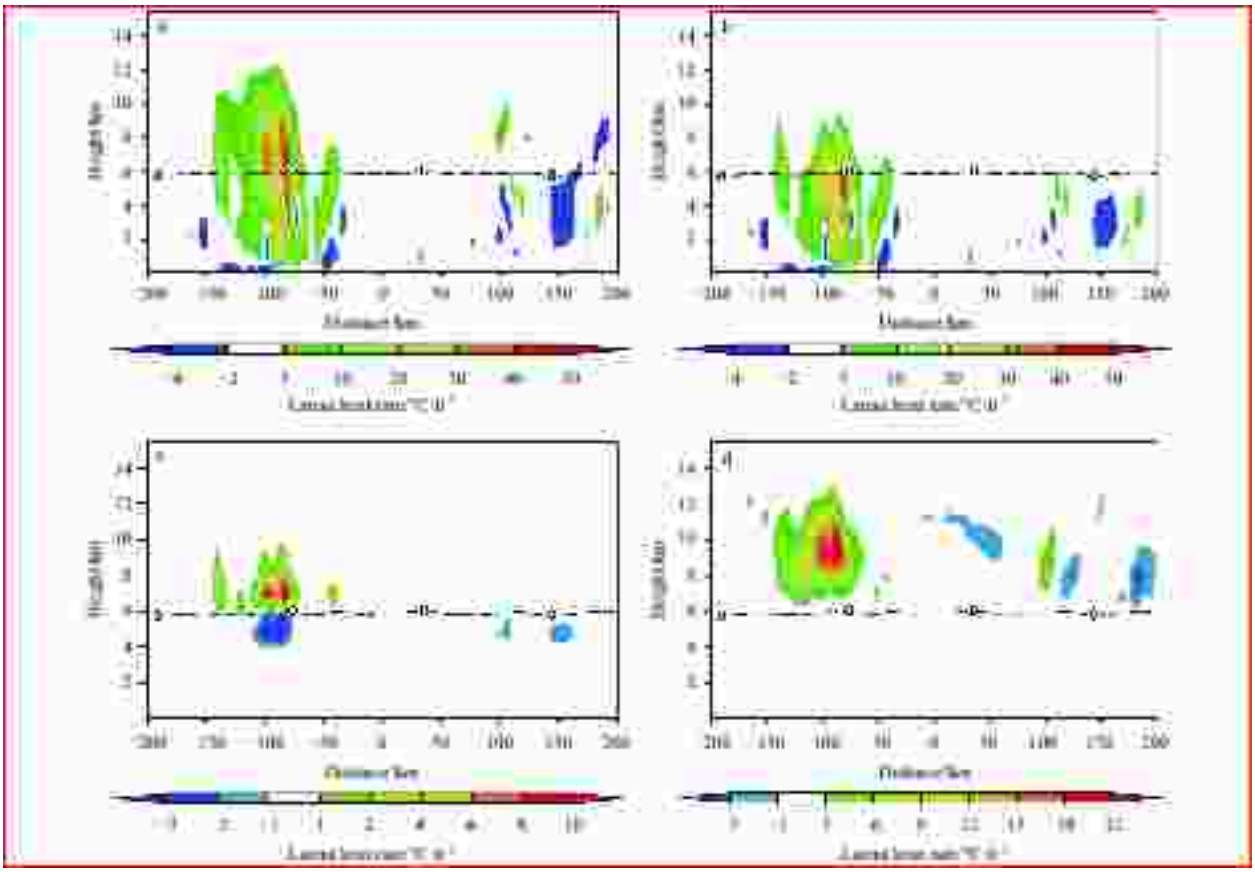

Fig. 7. An east-west cross-section through the center of Typhoon Molave showing various latent heating rates between 11:00 UTC on 18 July and 12:00 UTC on 18 July for the simulation. a. Total latent heat rate in Eq. (1); b. condensation and evaporation latent heat rate, $L_v(c–e)$; c. freezing and melting latent heat rate, $L_f(f–m)$; and d. deposition and sublimation latent heat rate, $L_s(d–s)$.

but concentrates below the zero degree isotherm. Above this isotherm, the LH rate for deposition and sublimation processes makes an important contribution to the total LH rate, and has a concentrated affect at 7–12 km height. The maximum LH rate for freezing and melting is 10 °C/h, at a position about 100 km west of the typhoon center in the simulation. Therefore, The condensation and evaporation have the positive contribution, and freezing and melting have the negative contribution to the latent heat of low level (below isotherm), while the freezing and melting, deposition and sublimation processes make an important contribution to latent heat of high level (above isotherm).

4.3.2 *The vertical profile of latent heat*

To analyze the LH profile, the simulated results were compared with satellite data from the TRMM (TMI) 2A12 at 07:15 UTC on 18 July. The selected domain ranges from 115.625°E to 117.625°E and from 20.125°N to 22.125°N. Figure 8 shows that there is a negative LH contribution to the total LH, concentrated below 500 m the height, which is mainly from rainwater evaporation. From 500 m to 4 km height, only condensation and evaporation contribute to the total LH profile. Over heights of 4–6 km, both positive condensation/evaporation and negative freezing/melting contribute to the LH. Deposition and sublimation mainly occur between 6 and 14 km, becoming a major contributor to LH at higher altitude.

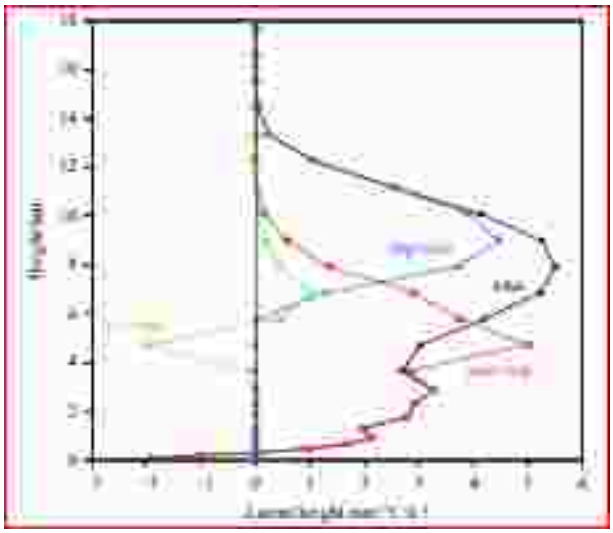

Fig. 8. Latent heating profiles of different microphysical processes for the simulation period from 07:00 to 07:30 UTC on 18 July. The black solid line represents the total latent heating profile, the red dotted line the condensation and evaporation (con plus evp) latent heating profile, the green dotted line the freezing and melting (frz plus mlt) latent heating profile, and the blue dotted line the deposition and sublimation (dep plus sub) latent heating profile.

Both differences and similarities exist between the simulated LH profile and the TRMM observation (Fig. 9). Overall, their vertical structures are similar. Both have negative LH rates near the surface and positive values above the zero degree isotherm. However, the peak values of the latent heat and its position within the column differ somewhat between the simulation and the observation. The maximum value of latent heat in the simulation is about 5.4°C/h at 7.8 km height, but for the TRMM observation,

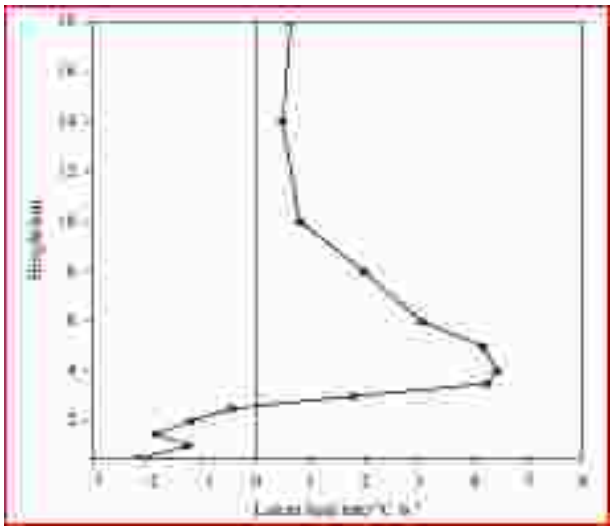

Fig. 9. Total latent heating profile for the TRMM 2A12 observation at 07:15 UTC on 18 July.

this peak value is 4.5°C/h at 4 km height. Moreover, a negative LH rate is observed from the surface to 2.5 km height in the TRMM data, but only exists below 500 m in the simulation. Finally, above 14 km height, the simulated LH rate is almost 0, while there is a small positive LH rate in the TRMM data. These discrepancies may result from differences in the algorithms used to determine the vertical structure of precipitation and the LH in both TRMM (Kummerow et al., 2001) and the WRF microphysical schemes.

4.4 *Analysis of latent heat from various cloud microphysical processes*

To determine the contribution of latent heat from various microphysical processes to the total latent heat, the integrated LH was calculated, as follows:

$$Q_x = \sum_{i,j,k} L_y \times P_x(i,j,k) \times \rho(i,j,k) \times \Delta x \times \Delta y \times \Delta z, \quad (2)$$

where Q_x is the LH release amount; L_y is the latent heat (L_v, L_f, L_s); $P_x(i, j, k)$ is the conversion rate of each cloud microphysical process; $\rho(i, j, k)$ is the air density; Δx and Δy are horizontal grid distances; and Δz is the vertical distance between any two model levels. The microphysical LH processes are listed in Tables 1 and 2. We used Domain D03 to calculate the integrated LH release amount per hour.

Tables 1 and 2 show the simulated magnitudes of the LH released for different cloud microphysical processes. The 13 positive microphysical processes are listed in Table 1, while the 12 negative ones are listed in Table 2. The largest LH contribution was from the condensation of cloud water (10^{18} J/h), although the deposition of cloud ice, deposition of snow, initiation of cloud ice crystals, deposition of graupel, and accretion of cloud water by graupel were also important contributors to the LH, reaching values of up to 10^{17} J/h. The magnitude of total LH release was 10^{18} J/h, which is comparable with values given in Adler and Rodgers (1977), and Gray (1981). For negative LH, the largest contribution was also from evaporation of cloud water, having a magnitude of 10^{18} J/h. Five negative LH microphysical processes reached values of up to 10^{17} J/h; these included evaporation of

Table 1. Magnitude of the various positive integrated latent heats released in the simulation

Positive latent heat release	Description of microphysical processes	Magnitude/J·h^{-1}
Q_{cond}	condensation of cloud water	10^{18}
Q_{idep}	deposition of cloud ice	10^{17}
Q_{sdep}	deposition of snow	10^{17}
Q_{igen}	initiation of cloud ice crystal	10^{17}
Q_{gdep}	deposition of graupel	10^{17}
Q_{gacw}	accretion of cloud water by graupel	10^{17}
Q_{revp} (>0)	condensation rate of rain	10^{16}
Q_{iacr}	accretion of rain by cloud ice	10^{16}
Q_{gacr}	accretion of rain by graupel	10^{16}
Q_{sacr}	accretion of rain by snow	10^{15}
Q_{ihmf}	homogeneous freezing of cloud water to form cloud ice	10^{14}
Q_{gfrz}	freezing of rain water to graupel	10^{13}
Q_{ihtf}	heterogeneous freezing of cloud water to form cloud ice	10^{12}

Table 2. Magnitude of the various negative integrated latent heats released in the simulation

Negative latent heat release	Description of microphysical processes	Magnitude/J·h^{-1}
Q_{evap}	evaporation of cloud water	10^{18}
Q_{revp} (<0)	evaporation of rain	10^{17}
Q_{ssub}	sublimation of snow	10^{17}
Q_{gsub}	sublimation of graupel	10^{17}
Q_{gmlt}	melting of graupel	10^{17}
Q_{isub}	sublimation of cloud ice	10^{17}
Q_{geml}	enhanced melting of graupel	10^{16}
Q_{smlt}	melting of snow	10^{16}
Q_{gevp}	evaporation of melting graupel	10^{16}
Q_{sevp}	evaporation of melting snow	10^{16}
Q_{seml}	enhanced melting of snow	10^{16}
Q_{imlt}	instantaneous melting of cloud ice	10^{14}

rain, sublimation of snow, sublimation of graupel, melting of graupel, and sublimation of cloud ice. Graupel had a marked influence on the LH release. In particular, the deposition of graupel, sublimation of graupel, accretion of cloud water by graupel, melting of graupel, and enhanced melting of graupel were important contributors to the LH.

5 Conclusions

This study introduces a new method for determining the latent heat using numerical simulations, which calculate LH rates for various microphysical processes. This is a markedly different approach from previous studies using the TRMM satellite retrieval.

Our comparison of the latent heat determined from the simulation versus the TRMM observations shows a similar overall structure, although specific values are different. The highest LH rate for the TRMM data is observed from 4 to 5 km, which is lower than the 8 km height obtained in the simulation. The total LH mainly originates from the condensation LH below the zero degree isotherm, and the deposition LH above it. Cloud microphysical processes related to graupel played a major role in our simulation. In our case study simulation of Typhoon Molave, we assessed the dominant contributors to the LH of various cloud microphysical processes. The positive contributors were mainly condensation of cloud water, deposition of cloud ice, deposition of snow, initiation of cloud ice crystals, deposition of graupel, and accretion of cloud water by graupel. The negative LH contributors were mainly evaporation of cloud water, evaporation of rain, sublimation of snow, sublimation of graupel, melting of graupel, and sublimation of cloud ice.

Acknowledgements

The authors thank the National Supercomputing Center in Guangzhou for providing the use of super-computers. We are grateful to the National Center for Atmospheric Research (NCAR) Mesoscale and Microscale Meteorology Division: http://www.mmm.ucar.edu/wrf/users, which is responsible for the WRF model. The National Centers for Environmental Prediction final (NCEP-FNL) global tropospheric analysis data for this paper are available at http://rda.ucar.edu/datasets/ds083.2.

References

Adler R F, Rodgers E B. 1977. Satellite-observed latent heat release in a tropical cyclone. Mon Wea Rev, 105(8): 956–963

Benjamin S O, Seaman N L. 1985. A simple scheme for objective analysis in curved flow. Mon Wea Rev, 113(7): 1184–1198

Betts A K. 1986. A new convective adjustment scheme: Part I. Observational and theoretical basis. Quart J Roy Meteor Soc, 112(473): 677–691

Dudhia J. 1989. Numerical study of convection observed during the winter monsoon experiment using a mesoscale two-dimensional model. J Atmos Sci, 46(20): 3077–3107

Emanuel K A. 1999. Thermodynamic control of hurricane intensity. Nature, 401(6754): 665–669

Gray W M. 1981. Recent advances in tropical cyclone research from rawindsonde composite analysis. World Meteorological Organization Programme on Research in Tropical Meteorology. Geneva, Switzerland: WMO, 407

Hogsett W, Zhang D L. 2009. Numerical simulation of hurricane bonnie (1998): Part III. Energetics. J Atmos Sci, 66(9): 2678–2696

Hong S Y, Lim J O J. 2006. The WRF single-moment 6-class microphysics scheme (WSM6). J Korean Meteor Soc, 42(2): 129–151

Hong S Y, Lim K S S, Kim J H, et al. 2009. Sensitivity study of cloud-resolving convective simulations with WRF using two bulk microphysical parameterizations: ice-phase microphysics versus sedimentation effects. J Appl Meteor Climatol, 48(1): 61–76

Hong S Y, Noh Y, Dudhia J. 2006. A new vertical diffusion package with an explicit treatment of entrainment processes. Mon Wea Rev, 134(9): 2318–2341

Houze R A Jr. 1997. Stratiform precipitation in regions of convection: A meteorological paradox. Bull Amer Meteor Soc, 78(10): 2179–2196

Janjić Z I. 1994. The step-mountain eta coordinate model: further developments of the convection, viscous sublayer, and turbulence closure schemes. Mon Wea Rev, 122(5): 927–945

Johnson R H. 1984. Partitioning tropical heat and moisture budgets into cumulus and mesoscale components: implications for cumulus parameterization. Mon Wea Rev, 112(8): 1590–1601

Kummerow C, Hong Y, Olson W S, et al. 2001. The evolution of the Goddard profiling algorithm (GPROF) for rainfall estimation from passive microwave sensors. J Appl Meteor, 40(11): 1801–1820

Fong S K, Wu C S, Hao I P, et al. 2001. Numerical prediction experiment on Typhoon Maggie (9903). Acta Oceanol Sinica, 20(2): 171–181

Lin W S, Xu S S, Sui C H. 2011. A numerical simulation of the effect of the number concentration of cloud droplets on Typhoon Chanchu. Meteor Atmos Phys, 113: 99–108

Low-Nam S, Davis C. 2001. Development of a tropical cyclone bogussing scheme for the MM5 system. In: Proceedings of the 11th PSU/NCAR Mesoscale Model User's Workshop. Colorado: Boulder, 130–134

Mlawer E J, Taubman S J, Brown P D, et al. 1997. Radiative transfer for inhomogeneous atmospheres: RRTM, a validated correlated-k model for the longwave. J Geophys Res, 102(D14): 16663–16682, doi: 10.1029/97JD00237

Molinari J, Dudek M. 1992. Parameterization of convective precipitation in mesoscale numerical models: a critical review. Mon Wea Rev, 120(2): 326–344

Olson W S, Kummerow C D, Hong Y, et al. 1999. Atmospheric latent heating distributions in the Tropics derived from satellite passive microwave radiometer measurements. J Appl Meteor, 38(6): 633–664

Pattnaik S, Krishnamurti T N. 2007. Impact of cloud microphysical processes on hurricane intensity: Part 2. Sensitivity experiments. Meteor Atmos Phys, 97(1–4): 127–147

Riehl H, Malkus J S. 1958. On the heat balance in the equatorial trough zone. Geophysica, 6: 503–538

Skamarock W C, Klemp J B, Dudhia J, et al. 2005. A description of the Advanced Research WRF version 2. NCAR Technical Note NCAR/TN-468+STR, 88

Sui C H, Lau K M, Tao W K, et al. 1994. The tropical water and energy cycles in a cumulus ensemble model: Part I. Equilibrium climate. J Atmos Sci, 51(5): 711–728

Tao W K, Lang S, Simpson J, et al. 1993. Retrieval algorithms for estimating the vertical profiles of latent heat release: their applications for TRMM. J Meteor Soc Japan, 71(6): 685–700

Tao W K, Smith E A, Adler R F, et al. 2006. Retrieval of latent heating from TRMM measurements. Bull Amer Meteor Soc, 87(11): 1555–1572

Wang L, Lau K H, Zhang Q H, et al. 2008. Observation of non-developing and developing tropical disturbances over the South China Sea using SSM/I satellite. Geophys Res Lett, 35(10): L10802, doi: 10.1029/2008GL033446

Wu C C, Cheng H J, Wang Y Q, et al. 2009. A numerical investigation of the eyewall evolution in a landfalling typhoon. Mon Wea Rev, 137(1): 21–40

Yanai M, Esbensen S, Chu J H. 1973. Determination of bulk properties of tropical cloud clusters from large-scale heat and moisture budgets. J Atmos Sci, 30(4): 611–627

Yang S, Smith E A. 1999. Moisture budget analysis of TOGA COARE area using SSM/I-retrieved latent heating and large-scale Q_2 estimates. J Atmos Oceanic Technol, 16(6): 633–655

Zhang D L, Kieu C Q. 2006. Potential vorticity diagnosis of a simulated hurricane: Part II. Quasi-balanced contributions to forced secondary circulations. J Atmos Sci, 63(11): 2898–2914